Electrochimica Acta 428 (2022) 140930

Contents lists available at ScienceDirect

Electrochimica Acta

journal homepage: www.journals.elsevier.com/electrochimica-acta

Multi-functional L-histidine self-assembled monolayers on SnO_2 electron transport layer to boost photovoltaic performance of perovskite solar cells

Xiaoxu Sun [a,b], Haipeng Jiang [c], Yansen Sun [a,b], Zonghan Guo [c], Zhenyu Pang [a,b], Fengyou Wang [c], Jinghai Yang [c,*], Lili Yang [c,*]

[a] Changchun Institute of Optics, Fine Mechanics and Physics, Chinese Academy of Sciences, Changchun 130033, PR China
[b] University of Chinese Academy of Sciences, Beijing 100049, PR China
[c] Key Laboratory of Functional Materials Physics and Chemistry of the Ministry of Education, Jilin Normal University, Changchun 130103, PR China

ARTICLE INFO

Keywords:
Perovskite solar cells
Self-assembly layer
Energy-level alignment
Coordination bond

ABSTRACT

The photovoltaic performance of perovskite solar cells (PSCs) is sensitive to the interface properties between perovskite and electron transport layer (ETL). An appropriate interface engineering on SnO_2 ETL is highly desired for achieving efficient PSCs. Herein, we introduced L-histidine (L-His) self-assembly layer on SnO_2 ETL to realize three following functions. The crystal quality and conductivity of SnO_2 ETL have been improved since the carboxyl groups in L-His coordinate with the tin ion in SnO_2 and fill the oxygen vacancy. The improved wettability caused by L-His deposition induces the formation of perovskite films with larger grain size and better crystallization quality. The hydrogen bond formed between perovskite and L-His proved by proton nuclear magnetic resonance (^{1}H NMR) enhances the interface interaction, and the L-His also modulates the energy level structure of the ETL/perovskite interface, which not only enhances the charge transport properties but also leads to a higher open-circuit voltage. Based on these benign optimizations, the $CH_3NH_3PbI_3$-based PSCs with the optimized SnO_2/L-His ETL have achieved a power conversion efficiency of 21.04%. Such biological friendly modification technique is highly compatibility to the technique of large-scale production of PSCs.

1. Introduction

Due to favorable optoelectronic properties including high absorption coefficients, long carrier diffusion lengths and high defect tolerance, organic-inorganic halide perovskites (OIHPs) have drawn remarkable attention in the field of perovskite light-emitting diodes and solar cell devices [1–4]. In recent years, the power conversion efficiency (PCE) of planar-type perovskite solar cells (PSCs) has been improved to 25.8% by optimizing the absorber materials, charge transporting layers and their interface [5]. The interface between electron transport layer (ETL) and perovskite plays a vital role in determining the overall photovoltaic performance of PSCs, since it positively influences the crystal quality of perovskite layer and the electron extraction/transport properties [6]. The SnO_2 has become a common ETL material for planar heterojunction cells due to its excellent advantages such as high transmittance, high carrier mobility and lower temperature preparation process [7]. However, pinholes and oxygen vacancy defects within SnO_2 films and especially the energy level mismatch between SnO_2 and perovskite still weaken the charge transport efficiency and interfacial stability. Due to the mismatch of energy levels and defects, the charge extraction efficiency at the SnO_2/perovskite interface is low and the carrier recombination is severe, resulting in low device efficiency and poor stability. The development of the additives or interlayers can not only improve the performance of the ETL, but also has a certain potential to affect the perovskite crystallization and reduce the recombination at the interface, which will help to improve the overall performance of the device. Therefore, optimizing the interface of the electron transport layer is an effective way to improve the photovoltaic performance of the device.

So far, various approaches have been used to modify the interface between ETL and perovskite, such as introducing multifunctional additives or inorganic/organic overlayers [8–15]. Researchers added some multifunctional additives into the SnO_2 precursor solution to realize simultaneous passivation of SnO_2, perovskite and interface defects through synergistic effect of anion and cation toward efficient and stable planar PSCs [12–14]. For instance, Zang group added LiOH into the SnO_2 layer and Li^+ doped into both perovskite and SnO_2 layers to

* Correspondence authors.
E-mail addresses: jhyang1@jlnu.edu.cn (J. Yang), llyang@jlnu.edu.cn (L. Yang).

https://doi.org/10.1016/j.electacta.2022.140930
Received 19 February 2022; Received in revised form 18 July 2022; Accepted 28 July 2022
Available online 28 July 2022

improve the carrier transport and extraction [13]. Similarly, our group also used potassium sodium tartrate with chelating function and K^+/Na^+ to synchronously optimize the SnO_2 layer, perovskite and interface with the help of K^+/Na^+ diffusion [15]. As for the inorganic/organic overlayers, Zhu et al. covered the SnO_2 ETL with KCl to improve the energy level arrangement and reduce the number of trap states, which effectively improved the charge extraction/transport and resulted in a higher PCE [10]. Hu et al. inserted the MACl layer between the SnO_2 ETL and perovskite layer to successfully accelerate the carrier extraction and transport and suppress the interfacial recombination, so that a very high open circuit voltage of 1.19 V has been finally achieved [12]. Our group also used CdS quantum dot layer to cover SnO_2 ETL to accelerate charge extraction and transfer for achieving highly efficient PSCs [11]. However, these methods suffered from more complicated process, higher preparation cost and certain toxicity. Therefore, more efforts should be taken to explore simpler technique and bio-friendly materials to optimize the interface between perovskite and SnO_2 ETLs.

Self-assembled monolayers (SAMs) have been proved to be a kind of powerful technique to manipulate chemical and physical interfacial properties for improving the performance of photoelectric devices, which also owns advantages of low cost and compatibility with large-scale preparation processes to satisfy the requirement of commercial application. So far, SAMs have been utilized to modify the interfaces of PSCs and the following positive effects have been exhibited [16,17]: (1) Appropriate SAMs covered on ETL can induce the growth of high-quality perovskite films with optimized morphology, better crystallinity, larger grain size and less defects. (2) Interfacial dipole moment can be well turned via modulating polarity of molecules, which helps to change the work function of ETL and build desired energy barrier at the interface to accelerate carrier extraction from the perovskite layer. (3) SAMs can passivate charge trap states on the interface and suppress the charge accumulation at the interface to reduce or eliminate device hysteresis.

In recent years, amino acids such as alanine ($C_3H_7NO_2$), glycine ($C_2H_5NO_2$) and L-cysteine ($C_3H_7NO_2S$) with great advantages of low-cost and good biocompatibility have been used as SAMs to modify ETL/perovskite interface layers to improve the photovoltaic performance of PSCs [18–20]. The bifunctional groups of -COOH and -NH_2 within amino acids have been proved to have ability to simultaneously cross-link the ETL and perovskite layers, leading to the faster interfacial charge extraction and transport. However, there are many kinds of amino acids, so that it is particularly important to choose the simpler and more effective one to well realize the above functions. Among them, L-Histidine ($C_6H_9N_3O_2$, L-His) was firstly considered due to the following reasons. From point view of the molecular structure, the biggest difference between L-His and alanine, glycine and L-cysteine mentioned above is that L-His has an imidazole ring. Considering the chemical structure of L-His, the oxygen atoms on the carboxyl group could coordinate with Sn^{4+} in SnO_2 nanoparticles to form a complex, which can promote the film quality of ETL to suppress the non-radiative recombination and improve the electron transfer and extraction efficiency at the ETL and interface [21]. The amino group can form hydrogen bonds with the organic cations of perovskite at the interface, which not only improves the compact interactions of the interface, but also improves the interfacial energy level matching, increases the charge extraction efficiency of the SnO_2/perovskite interface, and reduces the carrier complex [22]. Imidazole ring is an electron deficient aromatic ring with non centrosymmetric structure, which can generate intramolecular charge transfer to improve the chelation ability of molecules with Sn ions or Pb related defects at the ETL/Perovskite interface [23]. Thus, the L-His is able to exert stronger chelation and defect passivation ability, which is more beneficial for the improvement of photovoltaic performance of PSCs.

Herein, L-His was selected as a SAM buffer layer to modify SnO_2 ETL to enhance photovoltaic performance of PSCs. The crystal quality and photoelectric properties of both ETL and perovskite have been simultaneously improved. The interface charge transfer process has been greatly improved. After optimizing the concentration of L-His SAMs, the PCE of $MAPbI_3$ based PSCs can reach up to 21.04% with negligible hysteresis, enhanced stability and higher repeatability.

2. Experimental

Preparation of SnO_2 and SnO_2/L-His: The glass/ITO substrates were successively cleaned with deionized (DI) water, detergent, ethanol, acetone and isopropanol under ultrasonic condition for 30 min. Afterwards, all substrates were dried in an oven at 60° for 2 h, and then further cleaning with UV/Ozone (UV-O3) for 20 min to remove surface functional groups before use. The original SnO_2 precursor solution was prepared by diluting the SnO_2 colloidal dispersion with deionized (DI) water (volume ratio of 1:1) and stirring for 3 h. Dissolve L-His in 1 mL DI water and stir for 3 h to obtain L-His solution with different concentration. The original SnO_2 precursor solution was spin-coated on the ITO substrate at a speed of 5000 rpm for 30 s, and then annealed on a hot plate at 150 ℃ for 30 min to obtain the corresponding ETLs. In addition, the L-His solution was spin-coated on the ITO substrate at a speed of 5000 rpm for 30 s, and annealed on a hot plate at 150 ℃ for 20 min to obtain the buffer layer.

The fabrication process of PSCs and characterization conditions are similar with our previous reports [11,15], which can be found in the supporting information.

3. Results and discussion

To optimize the concentration of L-His, a series of PSCs with Glass/ITO/SnO_2/$CH_3NH_3PbI_3$/Spiro-OMeTAD/Ag structure (Fig. 1a) have been fabricated. Fig. S1 depicts the detailed preparation process of SnO_2/L-His/Perovskite films. The L-His with different concentration is spun coated between the ETL and the perovskite layer. The photovoltaic performance parameters for the L-His/SnO_2-based PSCs with different L-His contents are provided in Fig. S2. To check the reproducibility of PSCs, a batch of ten devices for each concentration of L-His was made. The average values in performances were obtained accordingly, which were then used to evaluate the experimental error. In the following analysis, the experimental error values were obtained by minus the average value and then divided by 2. According to Fig. S2, we can see that the optimal concentration of L-His is 0.06 mM, since the open circuit voltage (V_{oc}), short circuit current (J_{sc}) and fill factor (FF) of the devices are the highest at this concentration. In addition, forty devices were tested under standard light and the power conversion efficiency (PCE) of these PSCs at this concentration was generally higher. When the concentration of L-His is lower than 0.06 mM, L-His cannot completely and uniformly cover the rough SnO_2, which cannot make SnO_2 achieve a better dispersion and lead to a decrease in the electron transport capacity [24]. When the concentration of L-His increased to 0.08 mM, the excessive L-His can damage the charge carrier mobility of SnO_2 layer due to the poor conductivity of L-His [25], so that the PCE of -PSCs was reduced. The optimal concentration of 0.06 mM was then used for the following preparation of perovskite films and devices, which was named SnO_2/L-His based perovskite films and PSCs, respectively.

The effects of L-His on regulating the morphology and photoelectric properties of SnO_2 ETLs were subsequently explored. Firstly, we used scanning electron microscopy (SEM) and atomic force microscopy (AFM) to investigate the surface morphology of SnO_2 and SnO_2/L-His films. As shown in Fig. 1b and c, both films are compact without pinholes, but SnO_2/L-His film is flatter than SnO_2 film. Accordingly, the root-mean-square roughness (RMS) of SnO_2 and SnO_2/L-His films deduced from the AFM images in Fig. 1d and 1e is 1.4 nm and 1.1 nm, respectively. A slight decrease in roughness combined with SEM results prove that L-His effectively improve the uniformity and flatness of ETLs, preventing the direct contact between perovskite film and ITO electrode, which is beneficial for improving the charge transport capacity of SnO_2 ETL [26].

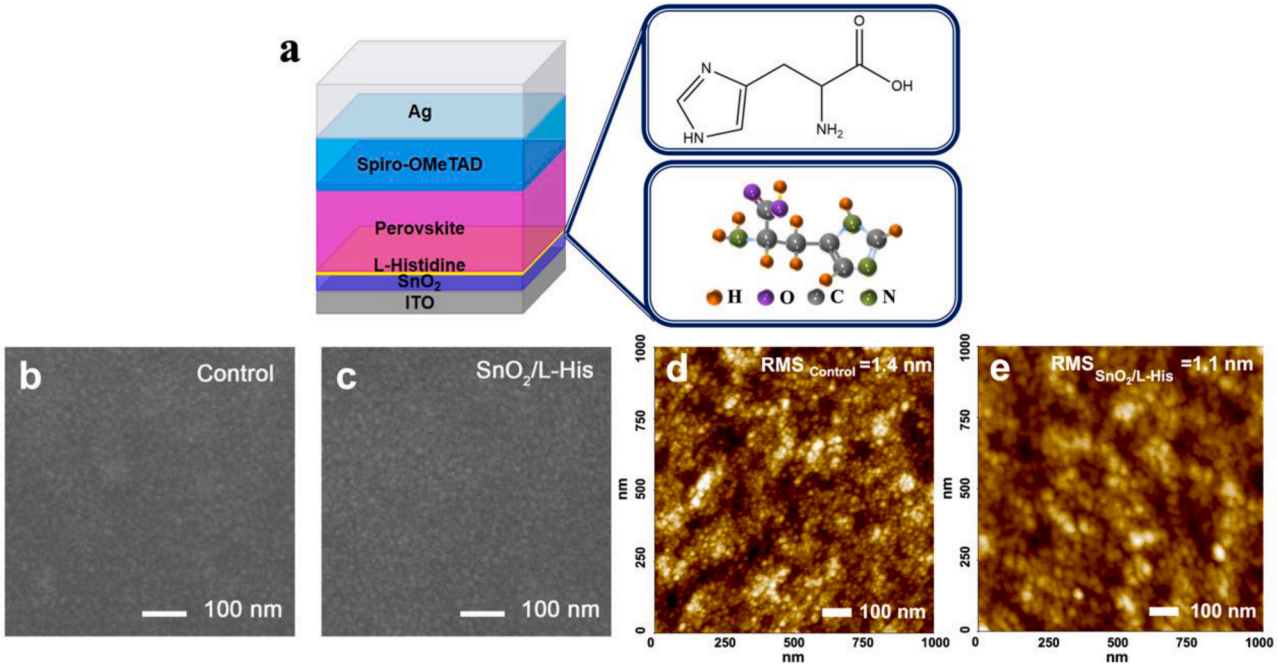

Fig. 1. Characterization of SnO_2/L-His ETL. a. Schematic diagram of the device structure with molecular structure of L-His. SEM images of **b.** SnO_2 and **c.** SnO_2/L-His. AFM images of **d.** SnO_2 and **e.** SnO_2/L-His.

Fig. S3 shows the XRD patterns of SnO_2 and SnO_2/L-His films deposited on soda lime glass at room temperature. The three diffraction peaks at 26.6°, 33.8° and 51.8° can be indexed to the (110), (101) and (211) crystal plane, respectively [27], indicating the formation of SnO_2 with tetragonal rutile structure according to PDF: No. 88–0287. The SnO_2/L-His peaks are essentially unchanged compared to the control sample, indicating that the L-His treatment does not change the crystal structure of SnO_2. Meanwhile, the similarity of UV–Vis transmittance spectra of SnO_2 and SnO_2/L-His films shown in Fig. S4 demonstrates that the L-His does not affect the light transmittance [28]. To illustrate the effect of L-His on the conductivity of SnO_2 ETL, the ETL only devices with architecture of ITO/SnO_2/Ag were fabricated. The corresponding current-voltage (I-V) curves are shown in Fig. S5. Obviously, the I-V curve of the L-His-modified SnO_2 ETL is steeper than that of the SnO_2 ETL. The conductivity of ETL film can be calculated using the following formula [29].

$$\sigma_0 = d/(AR) \tag{1}$$

where σ_0 is the conductivity, d is the thickness of the ETL, A is the activity area (0.09 cm^2), and R is the resistance [30]. Combining the cross-sectional SEM images in Fig. 3 and AFM height distribution measurements in Fig. S6, the thickness of SnO_2 and SnO_2/L-His film can be determined to be 23.2 nm and 24.3 nm, respectively. Thus, the calculated value of σ_0 for SnO_2 and SnO_2/L-His is 2.97×10^{-6} S cm^{-1} and 4.14×10^{-6} S cm^{-1}, respectively. Such obvious increase in conductivity indicates that the introduction of L-His can greatly improve the charge transport efficiency within the PSCs. Accordingly, the Hall Effect test (Fig. S7) also shows a decreasing tendency in resistivity. Therefore,

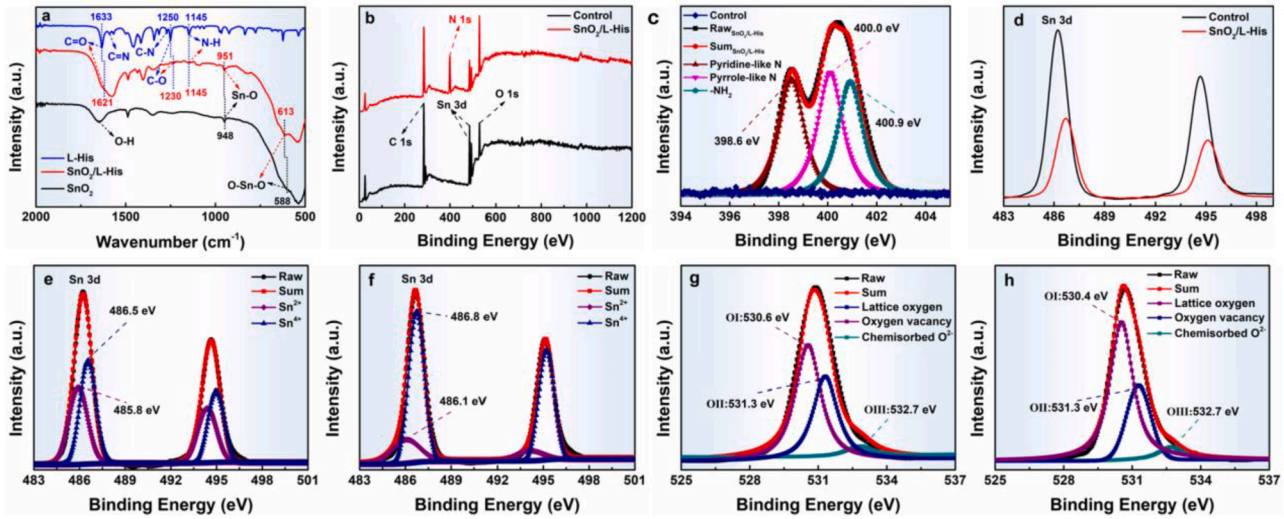

Fig. 2. The interaction between SnO_2 and L-His. a. FTIR spectra of SnO_2, L-His and SnO_2/L-His films. **b.** XPS survey spectra of SnO_2 and SnO_2/L-His films. **c.** High-resolution N 1 s XPS spectra of SnO_2 and SnO_2/L-His films. **d.** High-resolution Sn 3d XPS spectra of SnO_2 and SnO_2/L-His films. Fitting curves for Sn 3d XPS spectra of **e.** SnO_2 and **f.** SnO_2/L-His films. Fitting curves for O 1 s XPS spectra of **g.** SnO_2 and **h.** SnO_2/L-His films.

using L-His to modify SnO_2 simultaneously can improve the surface quality and enhance the electrical property, which not only provides a desired platform for depositing high quality perovskite films, but also brings expectation to achieve higher efficiency of charge extraction and collection [31].

Fourier transform infrared spectroscopy (FTIR) and X-ray photoelectron spectra (XPS) techniques were utilized to unveil the relative influence mechanism of L-His on SnO_2 for resulting in the above improvement. Fig. 2a shows the FTIR spectra of pure L-His, SnO_2 and SnO_2/L-His samples. As shown in the FTIR spectrum of SnO_2 colloidal dispersion in deionized water, the peaks located at 588 cm^{-1} and 948 cm^{-1} can be assigned to the stretching vibration of O-Sn-O and asymmetrical Sn-O stretching vibration modes, respectively. Besides, a strong band near 1650 cm^{-1} caused by O-H stretching vibration mode also appeared due to the existence of H_2O [32]. As shown in the FTIR spectrum of pure L-His powder, the characteristic vibrational peaks of C=O and C-O at 1633 and 1250 cm^{-1} have been illustrated, which are attributed to the stretching vibration caused by the carboxyl group in L-His [33]. The peak at 1145 cm^{-1} corresponds to the N-H vibrational stretching mode caused by the amino group [34]. Meanwhile, other two peaks located at 1590 and 1271 cm^{-1} are corresponding to the characteristic C=N and C-N vibrational peaks modes, respectively, which are originated from the imidazole ring in L-His [34]. Compared to these spectra, from the FTIR spectrum of the SnO_2/L-His sample, we can not only see the O-Sn-O and Sn-O peaks originated from SnO_2, but also the C=O, C-O, N-H and C-N peaks originated from L-His, indicating that the L-His is successfully modified on the SnO_2 films. Moreover, we can see that the N-H peak in SnO_2/L-His maintains at the initial position of L-His, indicating that the amino group of L-His does not interact with SnO_2 [32]. The C-N peak shifts to 1266 cm^{-1}, which can be ascribed to the formation of hydrogen bonds with water molecules [35]. It is worth to notice that the peaks of C=O, C-O in SnO_2/L-His shifted to 1621 and 1230 cm^{-1}, respectively. Accordingly, the peak of O-Sn-O and Sn-O in SnO_2/L-His shift to 613 and 951 cm^{-1}, respectively. Such obvious interactive shifts indicate that the chemical interaction between -COOH in L-His and SnO_2 have occurred [34].

To further testify it, the XPS survey spectra of SnO_2 and SnO_2/L-His films deposited on ITO substrates are shown in Fig. 2b. All spectra are all calibrated with the C 1s peak (284.8 eV). Besides Sn, O and C elements appeared in both samples, a strong N 1s peak at 400 eV also appears in the spectrum of SnO_2/L-His film. To see it clearly, the high-resolute scan N 1s XPS spectra of both samples are presented in Fig. 2c. After fitting, three peaks located at 398.6 eV, 400.0 eV and 400.9 eV can be assigned to pyridine-like N, pyrrole-like N and $-NH_2$ group [36], respectively, further proving the successful modification of L-His on SnO_2 film. Since the L-His belongs to Lewis base due to the existence of carboxyl group, the O atom in the carboxyl group contains two lone pairs of electrons, which possesses strong electronegativity to facilitate the coordination with Sn ion in SnO_2 [30]. To analyze the possible reaction that happens in SnO_2/L-His film, Sn 3d and O 1 s XPS spectra of SnO_2 and SnO_2/L-His are shown in Fig. 2d–h. Due to the asymmetry of both spectra, we further fitted Sn 3d XPS spectra with Gaussian-Lorentzian functions and presented them in Fig. 2e,f. Two deconvolution fitting peaks located at 486.5 eV and 485.8 eV are originated from Sn^{4+} and Sn^{2+}, respectively, indicating the coexistence of Sn^{4+} and Sn^{2+} in SnO_2 films [37]. The Sn^{2+} oxidation state is caused by the oxygen vacancies formed during spin coating, and its binding energy is higher than that of the Sn^{4+} oxidation state [38]. We calculated the relative ratio of Sn^{4+}/Sn^{2+}, and the peak intensity ratio of Sn^{4+}/Sn^{2+} increased from 1.98 for SnO_2 film to 3.71 for SnO_2/L-His film. Meanwhile, after depositing L-His on SnO_2, the Sn 3d peak position of Sn^{4+} and Sn^{2+} shifts to higher binding energy of 486.8 and 486.1 eV, respectively. Obviously, these results might because that the L-His brings the oxygen containing groups of -COOH into the SnO_2 films, which can coordinate with Sn^{4+} to effectively reduce the surface oxygen vacancies of SnO_2 films [39].

We then further provide the core-level lines of O 1 s of both SnO_2 films to unveil the detailed reasons for the reduced Sn^{2+} and Sn 3d peak shift. Fig. 2g shows a typical O 1 s XPS spectrum of pristine SnO_2, which can be fitted with three independent peaks at 530.5 eV, 531.3 eV, and 532.7 eV, corresponding to lattice oxygen (OI), oxygen vacancy (OII), and chemisorbed oxygen (OIII), respectively [40]. The peak intensity ratio of $I_{(OII)}/I_{(OI)}$ decreases from 0.62 of SnO_2 film to 0.54 of SnO_2/L-His film. Meanwhile, the OI peak of SnO_2/L-His film (Fig. 2h) exhibits an increase in the binding energy by about 0.2 eV. These results prove that the L-His modification effectively reduces the surface oxygen vacancies of SnO_2 films due to a chemical bonding reaction between Sn^{4+} and -COOH, which is also consistent with the results with FTIR.

Combining the results of FTIR and XPS spectra, Fig. S8 shows a schematic diagram of L-His passivation mechanism. As we know, the L-His structure has a strong electron-withdrawing group composed by a carboxyl group connected to an aromatic ring. Therefore, compared to the control SnO_2 film, the addition of L-His can increase the number of electrons around the Sn ions and prompt the chemical bonding reaction between Sn^{4+} and -COOH, which not only suppresses the oxygen vacancies, but also causes the binding energy of Sn ions move to the higher binding energy [41].

Effect on crystallization of perovskite films. In order to further study the effect of modified ETLs on perovskite films, Fig. 3a, b shows the top-view SEM images of perovskite films deposited on SnO_2 and SnO_2/L-His ETLs. A few pinholes appear on the SnO_2-based perovskite film. But the SnO_2/L-His based perovskite film contains continuous and regular perovskite grains with larger size. We further performed corresponding cross-sectional SEM images and showed them in Fig. 3c,d. Unsurprisingly, the SnO_2 based perovskite film shows a stratified structure with many small grains existing in the films. In contrast, the SnO_2/L-His based perovskite film shows columnar crystal grains from the bottom to the top. These columnar grains directly connect the ETL and hole transport layer (HTL), which facilitates the charge transport of perovskite layer [42]. The corresponding XRD patterns are shown in Fig. S9. Both samples show diffraction peaks at 14.2° and 28.4°, representing (100) and (220) lattice plane of perovskite with tetragonal structure, respectively [43]. The existence of L-His does not affect the crystal structure and growth orientation of $CH_3NH_3PbI_3$ crystals. It is noteworthy that the SnO_2/L-His based perovskite film owns stronger diffraction intensity, indicating a better crystallinity has been obtained [44], which is consistent with the variation tendency of SEM results. The mean crystals size in the primary crystal planes of the perovskite material is calculate by XRD analysis using Scherrer's formula:

$$D = K\lambda/(\beta\cos\theta) \tag{2}$$

where K is the Scherrer constant (0.89), D is the grain size (nm), β is the half-height width of the diffraction peak, which needs to be converted into radians (rad). θ is the glancing angle, λ is the X-ray wavelength (0.154056 nm) [45,46]. In order to make the data more accurate as well as comparable, we chose the (110), (220) and (310) diffraction main peaks to do the calculation. The mean crystal sizes of control and SnO_2/L-His based perovskite films is determined to be 30 nm and 34 nm, respectively. This particle size is also called the "subgrain size", which characterizes the "unit cell" size of the large grains to form the perovskite films. The increased subgrain size indicates that adding L-His at the interface can increase the grain size of the perovskite film and improve the crystalline quality [46].

Previous studies have shown that the nucleation process of perovskite is very sensitive to the surface energy of the substrate [47]. Then Fig. S10 shows the contact angle images of perovskite precursor solution on SnO_2 and SnO_2/L-His ETLs. Compared to the pristine SnO_2 ETL, the contact angle is reduced from 19.8° to 9.3° with introducing L-His layer. Such improved wettability facilitates the formation of the perovskite film [48,49]. In detail, the Gibbs free energy for heterogeneous nucleation can be expressed as Eq. (3):

$$\triangle G_{heterogeneous} = \triangle G_{homogeneous} \times f(\theta) \tag{3}$$

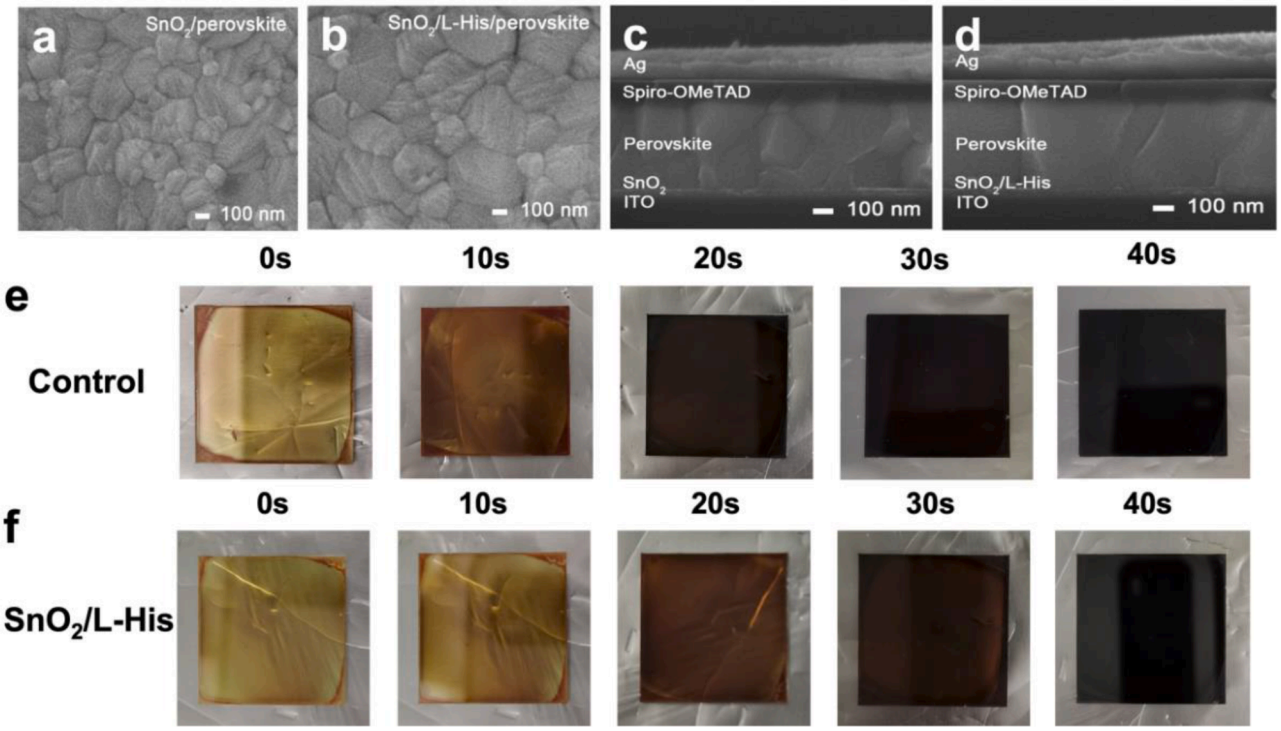

Fig. 3. Characterization of perovskite. Top-view scanning electron microscope (SEM) images of perovskite films coated on **a.** SnO_2 and **b.** SnO_2/L-His substrates. The cross-sectional SEM images of **c.** SnO_2-based and **d.** SnO_2/L-His-based complete planar-type PSCs devices. Photographs of the perovskite films **e.** without and **f.** with L-His collected at the subsequent delay times after posing the substrates on a hot plate at 100 ℃.

wherein $f(\theta) = (2–3\cos\theta + \cos^3\theta)/4$, and θ is the contact angle of the precursor solution [50]. Since the magnitude of θ varies in the range of [0, π/2], the larger the θ is, the larger parameter $f(\theta) \in [0, 1]$ is. In other words, the smaller contact angle makes the Gibbs free energy of heterogeneous nucleation lower, thereby resulting in the slower nucleation process, which is beneficial for obtaining larger grain size in perovskite films [51]. Obviously, the reduced Gibbs free energy caused by introducing L-His in our case is apt to retard the crystallization process [52]. To further prove it, we carried out the experiment in the glove box and collected the photographs of crystallization process of perovskite films every 10 s under 100℃ annealing conditions, which has been shown in Fig. 3e-f. It is clear that the SnO_2/L-His based perovskite films turn black slower than the control one. Therefore, a better crystallinity and enlarged grain size have been achieved in the perovskite deposited

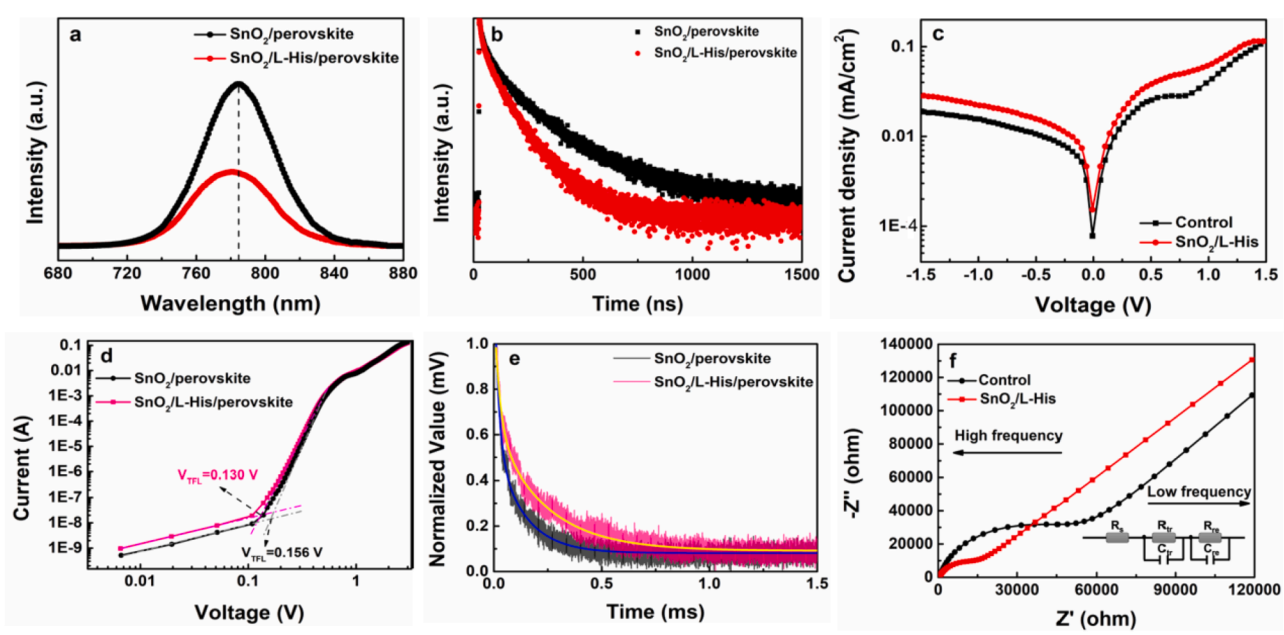

Fig. 4. Charge transport between perovskite and different ETLs. a. Steady-state PL and **b.** TRPL spectra of perovskite films deposited on SnO_2 and SnO_2/L-His ETLs. **c.** J-V characteristics of the SnO_2-device and SnO_2/L-His-device measured in the dark. **d.** Dark I-V curves of the electron-only devices. **e.** Transient photovoltage decay of SnO_2 and SnO_2/L-His based PSCs **f.** EIS of planar-type PSCs with different ETLs.

on the SnO_2/L-His [53]. Clearly, it exhibits the similar variation tendency as those under the atmospheric environment (Fig. S11), indicating that the L-His modification indeed delay the crystallization process of perovskite films.

Charge transfer dynamics. Fig. 4a shows the steady-state photoluminescence (PL) spectra of SnO_2/perovskite and SnO_2/L-His/perovskite. A significant PL quenching was observed in the SnO_2/L-His/perovskite compared to the control sample, which indicates that an efficient electron injection from perovskite into ETL has been achieved after introducing L-His on SnO_2 ETL [54]. In addition, the blue shift of the emission peak indicates that the defect states at the ETL/perovskite interface and the perovskite grain boundary are reduced, which is consistent with XRD and SEM results [55]. Fig. 4b shows the corresponding normalized time-resolved photoluminescence (TRPL) spectra. Both spectra can be fitted by a bi-exponent decay function of $I = A_1 \exp(-t/\tau_1)+A_2 \exp(-t/\tau_2)$. The detailed fitting parameters are shown in Table S1. The average lifetime of SnO_2/perovskite and SnO_2/L-His/-perovskite is 251.35 and 93.50 ns, respectively. Generally, the fast decay (τ_1) can be attributed to the quenching process caused by the charge separation and the slow decay (τ_2) can be attributed to the radiative recombination process of charge carriers [56]. Both τ_1 and τ_2 significantly decreased when the perovskite film is deposited on SnO_2/L-His, indicating that the electrons have been efficiently extracted from the perovskite layer into SnO_2/L-His and the charge separation and transport have been accelerated. Fig. 4c shows the dark J-V curves of SnO_2 and SnO_2/L-His based PSCs. The leakage current of the SnO_2/L-His based device is smaller than that of control device, indicating that the SnO_2/L-His based device can prevent leakage and improve the photovoltaic performance.

The electron trap density (N_t) within perovskite film is one of key factor to determine the charge transport process. Thus, the electron-only devices with the structure of ITO/ETL/perovskite/PCBM/Ag were fabricated to evaluate the N_t of perovskite deposited on different substrates. Fig. 4d shows the corresponding dark current voltage (I-V) curves of both devices based on SnO_2 and SnO_2/L-His ETLs. The linear correlation reveals an ohmic response at low bias voltages, and a nonlinear increase in current appears when the bias voltage is higher than the trap-filling limit voltage (V_{TFL}, Fig. 4d), indicating that the traps are completely filled. The N_t can be obtained from Eq. (4) [57]

$$N_t = 2\varepsilon_0 \varepsilon V/eL^2 \quad (4)$$

where L is the thickness of the perovskite film, q (1.602×10^{-19}C) is the elementary charge of the electron, ε_r (32) is the relative dielectric and ε_0 (8.8542×10^{-14} F/cm) is the vacuum permittivity. From the cross-sectional SEM images (Fig. 3c,d), the SnO_2-based perovskite film and SnO_2/L-His based perovskite film thickness can be determined to be about 458 nm and 464 nm, respectively. The N_t of the SnO_2 and SnO_2/L-His based perovskite film can be calculated to be 2.631×10^{15} cm^{-3} and 2.135×10^{15} cm^{-3}, respectively. The significantly reduced trap density greatly contributes to the faster charge separation and extraction [58].

Transient photovoltage decay (TPV) of PSCs under the open-circuit condition is another effective way to gain insight into the carrier recombination dynamics and free carrier lifetime within PSCs [59]. The TPV spectra of SnO_2 and SnO_2/L-His based PSCs were shown in Fig. 4e and the corresponding parameters are shown in Table S2. The charge-recombination lifetime (τ_v) of the SnO_2/L-His based device was substantially longer than that of the device based on pure SnO_2 (148 μs versus 76 μs), which is consistent with the slow charge recombination in the SnO_2/L-His based perovskite films derived from TRPL measurement [60]. These results further prove that introducing L-His on SnO_2 ETLs indeed gradually improves the crystal quality of ETL and perovskite films by passivating the defects.

The electrical impedance spectroscopy (EIS) was employed to obtain transfer resistance in the PSCs. Fig. 4f shows the Nyquist plots of PSCs based on SnO_2 and SnO_2/L-His ETLs measured under dark conditions with the equivalent circuit shown in the inset. The corresponding fitting parameters including series resistance (R_s), transfer resistance (R_{tr}), and recombination resistance (R_{rec}) are listed in Table S3. The R_s mainly reflects the electron transport capability, the high-frequency component is the signature of the R_{tr} and the low frequency component is characteristic of the R_{rec} [61]. It is worth noting that the SnO_2/L-His based device possesses a smaller Rs value compared with the control device. Meanwhile, it also has the smallest R_{tr} of 4.59×10^3 Ω and the largest R_{rec} of 4.29×10^7 Ω compared to the SnO_2-based PSCs. The smaller R_{tr} favors the extraction of electrons, while the large R_{rec} effectively resists charge recombination, which is consistent with the above observations. In our case, the perovskite/HTL interface is identical for both devices and the only factor affecting these resistances is the perovskite/ETL interface. Thus, SnO_2/L-His is further proved to be a desired ETL for planar PSC due to its great capacity to improve the charge transfer efficiency and suppress the recombination process.

The improvement of charge transport performance is usually related to the factors such as interface bonding and energy level matching. The L-His covered on the SnO_2 films is inevitably contact with perovskite precursor. To unveil the improvement of the charge transport performance of SnO_2/L-His based perovskite film, the liquid-state ^{1}H NMR spectra of perovskite precursors with and without L-His in deuterated Dimethyl sulfoxide-d6 (DMSO-d6) are depicted in Fig. 5a–c. Two single peaks at δ =7.34 ppm and δ=2.30 ppm can be attributed to the NH_3^+ and CH_3 of methylammonium, respectively [62]. Fig. 5b shows a typical peak of perovskite (2.30 ppm), indicating the introduction of L-His does not affect the chemical structure of perovskite. However, the introduction of L-His shifted the secondary peak of perovskite slightly (Fig. 5c, 7.32 ppm), proving that hydrogen bond has been formed between the hydrogen of L-His and the halide of perovskite, thus promoting charge transport performance [63]. The hydrogen bond interaction between perovskite and L-His is shown in Fig. 5d.

The degree of energy band matching at the interface between ETL and perovskite films also determines the kinetics of charge extraction and combination [64]. The L-His deposited on SnO_2 as SAM is inevitable to change the work function of ETLs. Therefore, the ultraviolet photoelectron spectroscopy (UPS) spectra of SnO_2 and SnO_2/L-His were performed and shown in Fig. 5e, f to evaluate their energy level. The cut-off binding energy ($E_{cut\ off}$) of SnO_2 and SnO_2/L-His is estimated to be 16.70 and 17.10 eV, respectively. Then, the Fermi level (E_F) of SnO_2 and SnO_2/L-His is calculated to be −4.52 and −4.12 eV using the equation $E_F = E_{cut\ off} - 21.22$ eV [65], respectively. The valence band maximum (VBM) of SnO_2 and SnO_2/L-His is 3.80 and 3.70 eV, respectively. Using the Tauc plot shown in Fig. 5g, the optical band gap (E_g) of SnO_2 and SnO_2/L-His is calculated to be 3.80 and 3.82 eV, respectively. Then the conduction band maximum (CBM) can be determined to be −4.52 and −4.00 eV. Based on these results, the possible energy level diagram of PSCs based on both ETLs has been illustrated in Fig. 5h. It can be seen that the increase of conduction band energy in SnO_2/L-His ELTs can reduce the band offset between $CH_3NH_3PbI_3$ and ETLs. Thus, the introduction of L-His layer successfully shifts the energy level of the SnO_2 ETLs and the Fermi level of SnO_2/L-His matched the conduction band of the perovskite well, which is another key factor to facilitate electron extraction and transport [66]. It also helps to achieve a higher open circuit voltage [67], which will be seen in the following discussion.

The photovoltaic performance of PSCs. With the superior optoelectronic properties discussed above, it is expected that the SnO_2/L-His would be a better ETL in the PSCs than the SnO_2. Therefore, planar PSCs were designed and fabricated based on different ETL. As shown in Fig. 6a, the J-V curves of planar PSCs based on different ETL with the key parameters including J_{sc}, V_{oc}, FF, and PCE summarized in the inset of Fig. 6a. The PCE of SnO_2 and SnO_2/L-His based PSCs is 20.05±0.17% and 21.04±0.14%, respectively. Fig. 6b shows the incident photon-to-charge conversion efficiency (IPCE) and the integrated current of the PSCs based on different ETLs. It is apparent that the device based on the SnO_2/L-His shows significantly higher IPCE. The integrated current

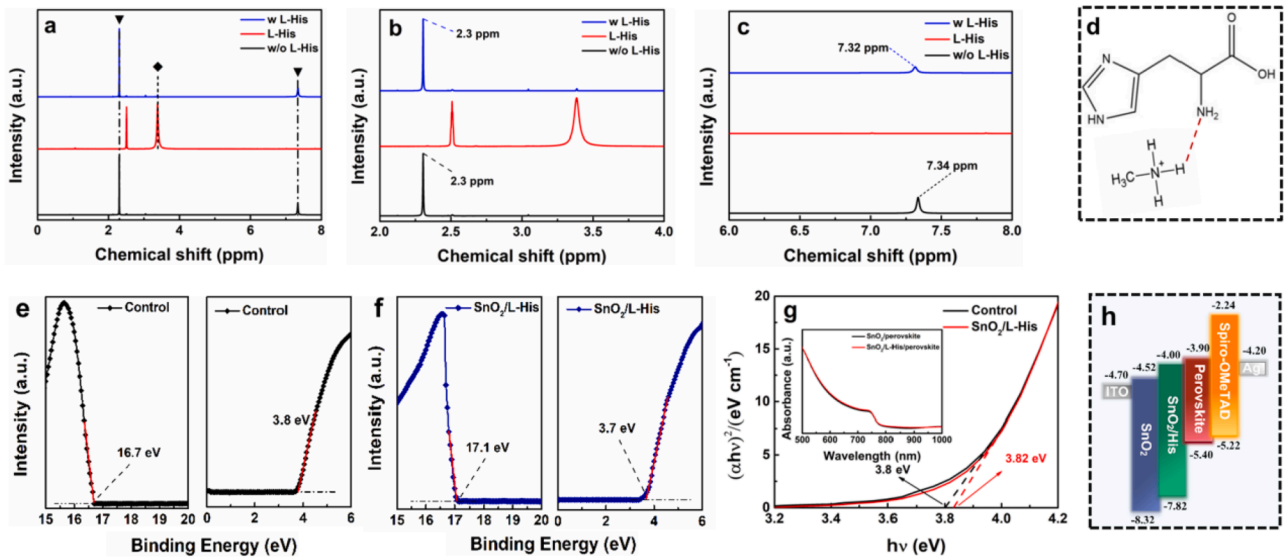

Fig. 5. Exploration of charge transport performance. a–c. Proton nuclear magnetic resonance (^{1}H NMR) analysis. ▼ represents the perovskite peak; ◆ represents the L-His peak. **d.** Schematic diagram of the hydrogen-bond formation between perovskite and L-His. UPS spectra of **e.** SnO_2 film and **f.** SnO_2/L-His film. **g.** Tauc plots of perovskite film deposited on SnO_2 and SnO_2/L-His film. The inset shows the UV–vis absorption spectra of perovskite films deposited on different substrates. **h.** Energy level diagram of PSCs.

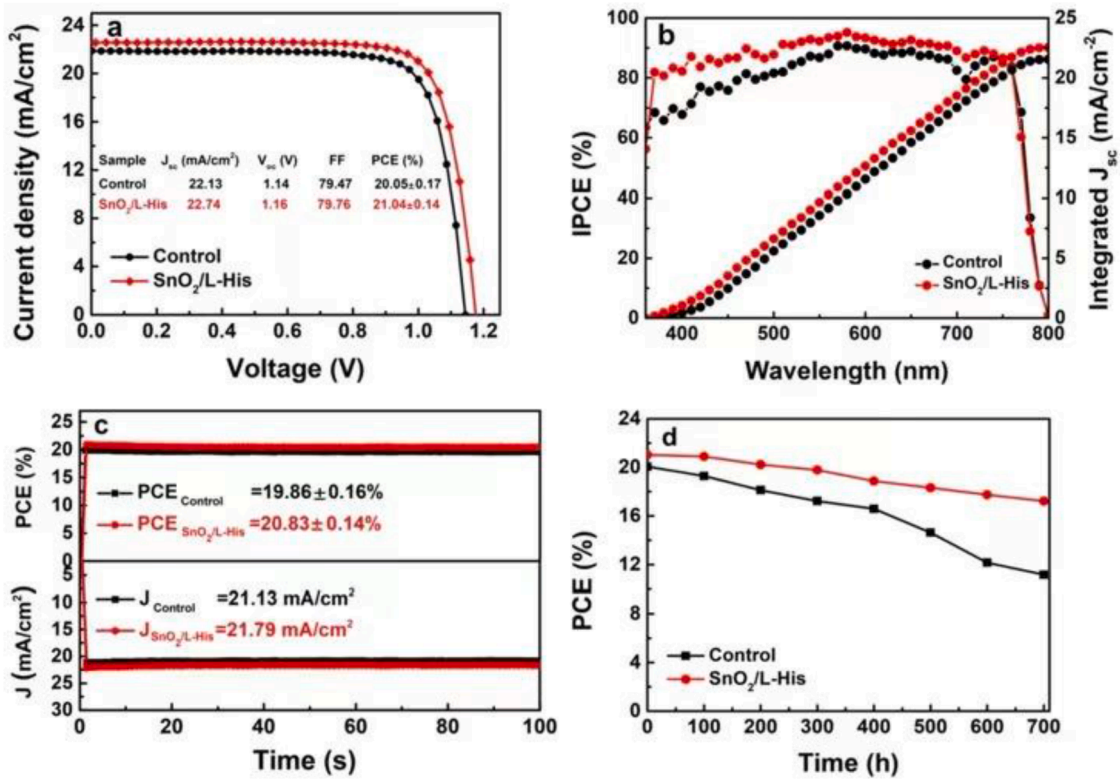

Fig. 6. The photovoltaic performance of SnO_2 and SnO_2/L-His based planar PSCs devices. a. The typical J–V curves of SnO_2 and SnO_2/L-His based PSCs. **b.** IPCE and integrated current density corresponding to planar PSCs with various ETLs. **c.** Variation of static current density and PCE measured with time. **d.** Long-term stability of PCE via storage time without any encapsulation under ambient condition.

value calculated by the IPCE spectra for the devices using SnO_2 and SnO_2/L-His are 21.82 and 22.43 mA/cm^2, respectively, which is very close to the J-V results [65].

Stability and hysteresis are two key characteristics of PSCs. Fig. S12 shows the J-V curves under reverse and forward scan. The hysteresis index (HI) calculated by HI = ($PCE_{reverse}$ - $PCE_{forward}$)/$PCE_{reverse}$ is 5.2% and 1% for SnO_2 and SnO_2/L-His based devices, respectively [68]. The J-V curves of PSCs based on SnO_2 ETLs showed a significant hysteresis. In general, the hysteresis of PSCs is attributed to the interfacial capacitance caused by the interfacial charge accumulation, which originates from ion migration, high trap density and unbalanced charge transport within the perovskite device [69]. According to the above results, both

the reduced trap density within devices and improved electron collection efficiency are reasonable to explain the hysteresis reduction [70].

The steady-state photocurrent density and PCE of the SnO_2 and SnO_2/L-His devices were further measured at the maximum power point. As shown in Fig. 6c, the PCE of PSCs based on the SnO_2 and SnO_2/L-His ETLs were stable at 19.86±0.16% and 20.83±0.14%, corresponding to photocurrent densities of 21.13 and 21.79 mA/cm^2, respectively. The photocurrent densities and PCE of both devices exhibit the negligible change under continuous solar illumination for 100 s, which proves excellent irradiation stability of the cells [70]. Fig. 6d shows the PCE variation curve via a function of storage time for unpackaged devices at 35% humidity and room temperature, and more detailed J-V parameters summarized in Table S4. It is clear that the SnO_2/L-His-based device maintains an initial efficiency of 82% in ambient air after 700 h, while the device of SnO_2-based device provides only 56% initial efficiency under the same storage conditions.

4. Conclusions

In summary, we propose a simple and effective method of L-His SAMs modification on SnO_2 ETL to comprehensively improve the photovoltaic performance of PSCs. First, the carboxyl group in L-His can coordinate with tin ions to fill the oxygen vacancies and improve the crystalline quality and conductivity of SnO_2 ETLs. Secondly, the introduction of L-His can improve the wettability of the interface and improve the crystallization of the perovskite film. Thirdly, the $-NH_2$ in L-His can form hydrogen bond between perovskite and L-His to enhance the charge transport performance. In addition, the introduction of L-His can also optimizes the energy level structure of the ETL/perovskite interface to further accelerate charge transfer. As a result, a maximum PCE of 21.04% with almost no hysteresis and enhanced stability in $CH_3NH_3PbI_3$-based PSCs has been achieved on the L-His-modified SnO_2 ETL. Such biological friendly modification technique is highly compatibility to the technique of large-scale production of PSCs, and the elucidation of relevant mechanisms in this work is very beneficial for understanding the functions of other amino acids in the future.

CRediT authorship contribution statement

Xiaoxu Sun: Formal analysis, Methodology, Investigation, Writing – original draft. **Haipeng Jiang:** Conceptualization, Investigation. **Yansen Sun:** Software. **Zonghan Guo:** Validation, Investigation. **Zhenyu Pang:** Software. **Fengyou Wang:** Conceptualization, Validation. **Jinghai Yang:** Resources, Supervision. **Lili Yang:** Resources, Supervision, Writing – review & editing.

Declaration of Competing Interest

The authors declare that they have no known competing financial interests or personal relationships that could have appeared to influence the work reported in this paper.

Acknowledgments

The authors would like to acknowledge financial support for this work from National Nature Science Foundation of China (Grant Nos. 22075101, 61904066, 11904127), Program for the development of Science and Technology of Jilin province (Item Nos. 20200801032GH, 20210509050RQ, 20210101410JC), the Thirteenth Five-Year Program for Science and Technology of Education Department of Jilin Province (Item Nos. JJKH20210440KJ, JJKH20200417KJ), and Construction Program for Innovation Research Team of Jilin Normal University (Grant No. 201703).

Supplementary materials

Supplementary material associated with this article can be found, in the online version, at doi:10.1016/j.electacta.2022.140930.

References

[1] J. Burschka, N. Pellet, S.J. Moon, R.H. Baker, P. Gao, M.K. Nazeeruddin, M. Gratzel, Sequential deposition as a route to high-performance perovskite-sensitized solar cells, Nature 499 (2013) 316–319, https://doi.org/10.1038/nature12340.

[2] N.J. Jeon, J.H. Noh, W.S. Yang, Y.C. Kim, S. Ryu, J. Seo, I.S. Sang, Compositional engineering of perovskite materials for high-performance solar cells, Nature 517 (2015) 476–480, https://doi.org/10.1038/nature14133.

[3] E. Pogna, M. Asgari, V. Zannier, L. Sorba, L. Viti, M.S. Vitiello, Unveiling the detection dynamics of semiconductor nanowire photodetectors by terahertz near-field nanoscopy, Light: Sci. Appl. 9 (2020) 12, https://doi.org/10.1038/s41377-020-00425-1.

[4] Y.X. Deng, S.X. Li, X.D. Li, R. Wang, X. Li, Green low-temperature-solution-processed *in situ* HI modified TiO_2/SnO_2 bilayer for efficient and stable planar perovskite solar cells build at ambient air conditions, Electrochim. Acta 326 (2019), 134924, https://doi.org/10.1016/j.electacta.2019.134924.

[5] H. Min, D. Lee, J. Kim, G. Kim, K.S. Lee, J. Kim, M.J. Paik, Y.K. Kim, K.S. Kim, M. G. Kim, et al., Perovskite solar cells with atomically coherent interlayers on SnO_2 electrodes, Nature 589 (2021) 444–450, https://doi.org/10.1038/s41586-021-03964-8.

[6] M. Aamir, T. Adhikari, M. Sher, N. Revaprasadu, Z.M. Nunzi, Fabrication of planar heterojunction $CsPbBr_2I$ perovskite solar cell using ZnO as electron transport layer & improved solar energy conversion efficiency, New J. Chem. 42 (2018) 14015–14670, https://doi.org/10.1039/c8nj02238k.

[7] Q. Dong, Y. Shi, C. Zhang, Y. Wu, L. Wang, Energetically favored formation of SnO_2 nanocrystals as electron transfer layer in perovskite solar cells with high efficiency exceeding 19%, Nano Energy 40 (2017) 336–344, https://doi.org/10.1016/j.nanoen.2017.08.041.

[8] Z. Lin, J. Yan, Q. Cai, X.N. Wen, H.Y. Dong, C. Mu, A sandwich-like electron transport layer to assist highly efficient planar perovskite solar cells, Nanoscale 11 (2019) 21917–21926, https://doi.org/10.1039/c9nr07876b.

[9] N. Dragomir, A. Igor, Optical metasurfaces: new generation building blocks for multi-functional optics, Light: Sci. Appl. 7 (2018) 58, https://doi.org/10.1038/s41377-018-0058-1.

[10] P. Zhu, S. Gu, X. Luo, Y. Gao, S.L. Li, J. Zhu, H. Tan, Simultaneous contact and grain-boundary passivation in planar perovskite solar cells using SnO_2-KCl composite electron transport layer, Adv. Energy Mater. 10 (2020), https://doi.org/10.1002/aenm.201903083, 1903083.1-1903083.7.

[11] Z. Lv, L. He, H.P. Jiang, X.J. Ma, F.Y. Wang, L. Fan, M.B. Wei, J.H. Yang, L.L. Yang, N.N. Yang, Diluted-CdS quantum dot-assisted SnO_2 electron transport layer with excellent conductivity and suitable band alignment for high-performance planar perovskite solar cells, ACS Appl. Mater. Inter. 13 (2021) 16326–16335, https://doi.org/10.1021/acsami.1c00896.

[12] X.F. Hu, H.X. Wang, Y.S. Ying, M. Wang, C. Zhang, Y.Q. Ding, H.Y. Li, W. Li, S. Y. Zhao, Z.G. Zang, Methylammonium chloride as an interface modificator for planar-structure perovskite solar cells with a high open circuit voltage of 1.19V, J. Power Sources 480 (2020), 229073, https://doi.org/10.1016/j.jpowsour.2020.229073.

[13] Q.X. Zhuang, H.X. Wang, C. Zhang, C. Gong, H.Y. Li, J.Z. Chen, Z.G. Zang, Ion diffusion-induced double layer doping toward stable and efficient perovskite solar cells, Nano Res. 15 (2022) 5114–5122, https://doi.org/10.1007/s12274-022-4135-7.

[14] C. Zhang, H.X. Wang, H.Y. Li, Q.X. Zhuang, C. Gong, X.F. Hu, W.S. Cai, S.Y. Zhao, J.Z. Chen, Z.G. Zang, Simultaneous passivation of bulk and interface defects through synergistic effect of anion and cation toward efficient and stable planar perovskite solar cells, J. Energy Chem. 63 (2021) 452–460, https://doi.org/10.1016/j.jechem.2021.07.011.

[15] Y.S. Sun, Z.Y. Pang, Y.N. Quan, D.L. Han, X.Y. Zhang, X. Ge, F.Y. Wang, Y.F. Sun, J. H. Yang, L. L.Yang, A synchronous defect passivation strategy for constructing high-performance and stable planar perovskite solar cells, Chem. Eng. J. 413 (2021), 127387, https://doi.org/10.1016/j.cej.2020.127387.

[16] F. Ali, R.C. Cristina, M. Sohail, M.K. Nazeeruddin, Applications of self-assembled monolayers for perovskite solar cells interface engineering to address efficiency and stability, Adv. Energy Mater. 10 (2020), 2002989, https://doi.org/10.1002/aenm.202002989.

[17] Z.H. Dai, S.K. Yadavalli, M. Chen, A. Abbaspourtamijani, Y. Qi, N.P. Padture, Interfacial toughening with self-assembled monolayers enhances perovskite solar cell reliability, Science 372 (2021) 618–622, https://doi.org/10.1126/science.abf5602.

[18] S.Q. Han, H.M. Zhang, Y.J. Li, R.F. Wang, Q.C. He, Solution-processed amino acid modified SnO_2 electron transport layer for carbon-based $CsPbIBr_2$ perovskite solar cells, Mat. Sci. in Semicon. Proc. 133 (2021), 105964, https://doi.org/10.1016/j.mssp.2021.105964.

[19] C.T. Lin, W.D. Xu, T.J. Macdonald, J. Ngiam, J.H. Kim, T. Du, S.D. Xu, P. S. Tuladhar, H.K. Kang, K. Lee, J.R. Durrant, M.A. McLachlan, Correlating the active layer structure and composition with the device performance and lifetime of amino-acid-modified perovskite solar cells, ACS Appl. Mater. Interfaces 13 (2021) 43505–43515, https://doi.org/10.1021/acsami.1c08279.

[20] R.J. Hu, W.J. Hou, G.Y. Han, T. Ou, Y.Z. Chang, Y.M. Xiao, Interfacial chemical bridge constructed by L-cysteine for highly efficient perovskite solar cells, Mater. Res. Bull. 149 (2022), 111698, https://doi.org/10.1016/j.materresbull.2021.111698.

[21] J.H. Du, L.P. Feng, X. Guo, X.P. Huang, Z.H. Lin, J. Su, Z.S. Hu, J.C. Zhang, J. J. Chang, Y. Hao, Enhanced efficiency and stability of planar perovskite solar cells by introducing amino acid to SnO_2/perovskite interface, J. Power Sources. 455 (2020), 227974.

[22] J.L. Du, Y.L. Wang, Y. Zhang, G.Y. Zhao, Y.W. Jia, X.T. Zhang, Y.C. Liu, Ionic liquid-assisted improvements in the thermal stability of $CH_3NH_3PbI_3$ perovskite photovoltaics, Phys. Status Solidi R. 12 (2018), 1800130, https://doi.org/10.1016/j.jpowsour.2020.227974.

[23] J.Y. Feng, K.W. Lai, Y.S. Shiue, A. Singh, C.P. Kumar, C.T. Li, W.T. Wu, J.T. Lin, C. W. Chu, C.C. Chang, C.C. Su, Cost-effective dopant-free star-shaped oligo-aryl amines for high performance perovskite solar cells, J. Mater. Chem. A. 7 (2019) 14209–14221, https://doi.org/10.1039/c9ta01278h.

[24] H.J. Liu, H. Bala, B. Zhang, B.B. Zong, L.W. Huang, W.Y. Fu, G. Sun, J.L. Cao, Z. Y. Zhan, Thickness-dependent photovoltaic performance of TiO_2 blocking layer for perovskite solar cells, J. Alloy. Compd. 736 (2018) 87–92, https://doi.org/10.1016/j.jallcom.2017.11.081.

[25] M.Y. Zhang, F.M. Wu, D. Chi, K.L. Shi, S.H. Huang, High-efficiency perovskite solar cells with poly(vinylpyrrolidone)-doped SnO_2 as an electron transport layer, Adv. Mater. 1 (2020) 617–624, https://doi.org/10.1039/D0MA00028K.

[26] Y.K. Noh, J.H. Lee, I.S. Jin, S.H. Park, J.W. Jung, Enhanced efficiency and ambient stability of planar heterojunction perovskite solar cells by using organic-inorganic double layer electron transporting material, Electrochim. Acta 294 (2019) 337–344, https://doi.org/10.1016/j.electacta.2018.10.138.

[27] K. Keis, E. Magnusson, H. Lindstrom, S.E. Lindquist, A. Hagfeldt, A 5% efficient photoelectrochemical solar cell based on nanostructured ZnO electrodes, Sol. Energy Mat. Sol. C 73 (2002) 51–58, https://doi.org/10.1016/S0927-0248(01)00110-6.

[28] Y.W. Jang, S. Lee, K.M. Yeom, K. Jeong, K. Choi, M. Choi, J.H. Noh, Intact 2D/3D halide junction perovskite solar cells via solid-phase in-plane growth, Nat. Energy 6 (2021) 63, https://doi.org/10.1038/s41560-020-00749-7.

[29] Y. Qiang, Y.H. Xie, Y. Qi, P. Wei, H.K. Shi, C. Geng, H.C. Liu, Enhanced performance of carbon-based perovskite solar cells with a Li^+-doped SnO_2 electron transport layer and Al_2O_3 scaffold layer, Sol. Energy 201 (2020) 523–529, https://doi.org/10.1016/j.solener.2020.03.046.

[30] Y.S. Sun, Z.Y. Pang, Y.N. Quan, D.L. Han, X.Y. Zhang, X. Ge, F.Y. Wang, Y.F. Sun, J. H. Yang, L.L. Yang, A synchronous defect passivation strategy for constructing high-performance and stable planar perovskite solar cells, Chem. Eng. J. 413 (2020), 127387, https://doi.org/10.1016/j.cej.2020.127387.

[31] Y. Chen, H.T. Yi, X. Wu, R. Haroldson, Y.N. Gartstein, Y.I. Rodionov, K. S. Tikhonov, A. Zakhidov, X.Y. Zhu, V. Podorov, Extended carrier lifetimes and diffusion in hybrid perovskites revealed by Hall effect and photoconductivity measurements, Nat. Commun. 7 (2016) 12253, https://doi.org/10.1038/ncomms12253.

[32] H.Q. Zhan, C. Deng, Q. Liu, X.H. Li, Z.P. Xie, C.A. Wang, Growth process, photoluminescence property and photocatalytic activity of SnO_2 nanorods, Chin. J. Inorg. 36 (2020) 1605–1612, https://doi.org/10.11862/CJIC.2020.176.

[33] Y.D. Ming, Y.Q. Zhu, Y. Chen, B.W. Jin, C.H. Duan, Z.H. Liang, L. Zhao, S.M. Wang, B.H. Dong, H.J. Li, C.C. Wu, β-alanine-anchored SnO_2 inducing facet orientation for high-efficiency perovskite solar cells, ACS Appl. Mater. Interfaces 13 (2021) 57163–57170, https://doi.org/10.1021/acsami.1c17260.

[34] J. Sukprasert, K. Thumanu, I. Phung-on, C. Jirarungsatean, L.E. Erickson, P. Tuitemwong, K. Tuitemwong, Synchrotron FTIR light reveals signal changes of biofunctionalized magnetic nanoparticle attachment on salmonella sp, J. Nanomater. 6 (2020) 1–12, https://doi.org/10.1155/2020/6149713.

[35] H.Y. Zheng, G.Z. Liu, W.W. Wu, H.F. Xu, X. Pan, Effective interface defect passivation via employing 1-methylbenzimidazole for highly efficient and stable perovskite solar cells, ChemSusChem 14 (2021) 3147–3154, https://doi.org/10.1002/cssc.202101097.

[36] Q. Zhou, L.S. Liang, J.J. Hu, B.B. Cao, L.K. Yang, T.J. Wu, X. Li, B. Zhang, P. Gao, High-performance perovskite solar cells with enhanced environmental stability based on a $(p\text{-}FC_6H_4C_2H_4NH_3)_2[PbI_4]$ capping layer, Adv. Energy Mater. 9 (2019), 1802595, https://doi.org/10.1002/aenm.201802595.

[37] P. Chen, Y. Bai, S.C. Wang, M.Q. Lyu, J.H. Yun, L.Z. Wang, *In situ* growth of 2D perovskite capping layer for stable and efficient perovskite solar cells, Adv. Funct. Mater. 14 (2018), 1706923, https://doi.org/10.1002/adfm.201706923.

[38] H.B. Wang, Y. Qiang, S.S. Zheng, P. Wei, Y.H. Xie, Enhanced efficiency and stability of carbon-based perovskite solar cells by Eva interface engineering, Adv. Mater. Interfaces 9 (2022), 2001076, https://doi.org/10.1002/ente.202001076.

[39] X.L. Liu, L.Q. Kong, H.M. Du, Y. Zhang, J.S. Zhao, Y. Xie, Synthesis and electrochromic properties of electrochromic polymers based on propylenedioxythiophene, diketopyrrolopyrrole and benzodithiophene units, Org. Electron. 64 (2019) 223–235, https://doi.org/10.1016/j.orgel.2018.10.035.

[40] V.H. Tran, S.K. Kim, S.H. Lee, Zwitterion nondetergent sulfobetaine-modified SnO_2 as an efficient electron transport layer for inverted organic solar cells, ACS Omega 4 (2019) 19225–19237, https://doi.org/10.1021/acsomega.9b02551.

[41] W.L. Jiang, Q.S. Dong, N. Li, L.D. Wang, Direct evidence of ion diffusion for the silver-electrode-induced thermal degradation of inverted perovskite solar cells, Adv. Energy Mater. 7 (2017), 1602922, https://doi.org/10.1002/aenm.201602922.

[42] R. Tao, Y.Z. Zhang, Z.B. Jin, Z.X. Sun, L. Xu, Polyoxometalate doped tin oxide as electron transport layer for low cost, hole-transport-material-free perovskite solar cells, Electrochim. Acta 284 (2018) 10–17, https://doi.org/10.1016/j.electacta.2018.07.157.

[43] L.L. Yan, S.L. Huang, H.Z. Ren, D.K. Zhang, W.Z. Liu, Y. Zhao, X.D. Zhang, Bifunctional CO_2 plasma treatment at i/p interface enhancing performance of planar silicon heterojunction solar cell, Phys. Status Solidi R. 1 (2021), 2100010, https://doi.org/10.1002/pssr.202100010.

[44] Z.G. Xiao, Q.F. Dong, C. Bi, Y.C. Shao, Y.B. Yuan, J.S. Huang, Solvent annealing of perovskite-induced crystal growth for photovoltaic-device efficiency enhancement, Adv. Mater. 26 (2015) 6503–6509, https://doi.org/10.1002/adma.201401685.

[45] Y. Long, K. Liu, Y. Zhang, W. Li, Ambient air temperature assisted crystallization for inorganic $CsPbI_2Br$ perovskite solar cells, Molecules 26 (2021) 3398, https://doi.org/10.3390/molecules26113398.

[46] Y. Luo, X. Yan, J. Zhang, B. Li, Y. Wu, Q. Lu, C. Jin, X. Zhang, X. Ren, A graphene/single GaAs nanowire Schottky junction photovoltaic device, Nanoscale 10 (2018) 9212–9217, https://doi.org/10.1039/c8nr00158h. PMID29726561.

[47] S. Liu, Y.W. Du, C.Y. Tso, H.H. Lee, R. Cheng, S.P. Feng, K.M. Yu, Thermochromic smart windows: organic hybrid perovskite ($MAPbI_{3-x}Cl_x$) for thermochromic smart window with strong optical regulation ability, low transition temperature, and narrow hysteresis width, Adv. Funct. Mater. 31 (2021), 2170186, https://doi.org/10.1002/adfm.202170186.

[48] E.H. Jung, B. Chen, K. Betens, M. Vafaie, S. Teale, A. Proppe, Y. Hou, T. Zhu, C. Zheng, E.H. Sargent, Bifunctional surface engineering on SnO_2 reduces energy loss in perovskite solar cells, ACS Energy Lett. 5 (2020) 2796–2801, https://doi.org/10.1021/acsenergylett.0c01566.

[49] P.C. Zhu, S. Gu, X. Luo, Y. Gao, S.L. Li, J. Zhu, H.R. Tan, Simultaneous contact and grain-boundary passivation in planar perovskite solar cells using SnO_2-KCl composite electron transport layer, Adv. Energy Mater. 10 (2020), https://doi.org/10.1002/aenm.201903083, 1903083.1-1903083.

[50] H. Zhao, S. Wang, M. Sun, F. Zhang, X.G. Li, Y. Xiao, Enhanced stability and optoelectronic properties of $MAPbI_3$ films by a cationic surface-active agent for perovskite solar cells, J. Mater. Chem. A 6 (2018) 10825–10834, https://doi.org/10.1039/C8TA00457A.

[51] T. Salim, S.Y. Sun, Y. Abe, A. Krishna, A.C. Grimsdale, Y.M. Lam, Perovskite-based solar cells: impact of morphology and device architecture on device performance, J. Mater. Chem. A 3 (2014) 8943–8969, https://doi.org/10.1039/c4ta05226a.

[52] L. He, Z. Lv, H.P. Jiang, X.J. Ma, F.Y. Wang, L. Fan, M.B. Wei, J.H. Yang, L.L. Yang, H.L. Liu, Sandwich-like electron transporting layer to achieve highly efficient perovskite solar cells, J. Power Sources. 453 (2020), 227876, https://doi.org/10.1016/j.jpowsour.2020.227876.

[53] P. Fu, L.Q. Huang, W. Yu, D. Yang, G.J. Liu, L.Y. Zhou, J. Zhang, C. Li, Efficiency improved for inverted polymer solar cells with electrostatically self-assembled BenMelm-CI ionic liquid layer as cathode interface layer, Nano Energy 13 (2015) 275–282, https://doi.org/10.1016/j.nanoen.2015.02.032.

[54] W.Y. Zhang, X.Y. Zheng, Y.C. Li, L. He, X. Li, Gourmet powder functionalization of SnO_2 for high-performance perovskite solar cells made in air, Electrochim. Acta 371 (2021), 137812, https://doi.org/10.1016/j.electacta.2021.137812.

[55] S. Yang, J.C. Yao, Y.N. Quan, M.Y. Hu, R. Su, M. Gao, D.L. Han, J.H. Yang, Monitoring the charge-transfer process in a Nd-doped semiconductor based on photoluminescence and SERS technology, Light: Sci. Appl. 9 (2020) 7, https://doi.org/10.1038/s41377-020-00361-0.

[56] Y.W. Li, L. Meng, Y. Yang, G.Y. Xu, Z.R. Hong, Q. Chen, J.B. You, G. Li, Y. Yang, Y. F. Li, High-efficiency robust perovskite solar cells on ultrathin flexible substrates, Nat. Commun. 7 (2016) 10214, https://doi.org/10.1038/ncomms10214.

[57] J.S. Yun, J. Seidel, J. Kim, A.M. Soufiani, S.J. Huang, J. Lau, N.J. Jeon, S. Seok, M. A. Green, A. Ho-Baillie, Critical role of grain boundaries for ion migration in formamidinium and methylammonium lead halide perovskite solar cells, Adv. Energy Mater. 6 (2016), 1600330, https://doi.org/10.1002/aenm.201600330.

[58] Y.C. Liu, J.K. Sun, Z. Yang, D. Yang, X.D. Ren, H. Xu, Z. Yang, S.Z. Liu, 220-mm-Large single-crystalline formamidinium-perovskite wafer for mass production of integrated photodetectors, Adv. Opt. Mater. 4 (2016) 1829–1837, https://doi.org/10.1002/adom.201600327.

[59] L. Meng, C.K. Sun, R. Wang, W.C. Huang, Z.P. Zhao, P.Y. Sun, T.Y. Huang, J.J. Xue, J.W. Lee, C.H. Zhu, et al., Tailored phase conversion under conjugated polymer enables thermally stable perovskite solar cells with efficiency exceeding 21%, J. Am. Chem. Soc. 140 (2018) 17255–17262, https://doi.org/10.1021/jacs.8b10520.

[60] Q.S. Dong, C. Zhu, M. Chen, C. Jiang, J.Y. Guo, Y.L. Feng, Z.H. Dai, S.K. Yadavalli, M.Y. Hu, X. Cao, et al., Interpenetrating interfaces for efficient perovskite solar cells with high operational stability and mechanical robustness, Nat. Commun. 12 (2021) 973, https://doi.org/10.1038/s41467-021-21292-3.

[61] J.Y. Chen, Z.N. Bi, X.Q. Xu, H.Z. Yu, The low temperature solution-processable SnO_2 modified by Bi_2O_2S as an efficient electron transport layer for perovskite solar cells, Electrochim. Acta 330 (2020), 135197, https://doi.org/10.1016/j.electacta.2019.135197.

[62] M. Mas-Montoya, D. Curiel, J.K. Wang, B.J. Bruijnaers, R.A.J. Janssen, Use of sodium diethyldithiocarbamate to enhance the open-circuit voltage of $CH_3NH_3PbI_3$ perovskite solar cells, Solar RRL 5 (2021), 2000811, https://doi.org/10.1002/solr.202000811.

[63] K. Liu, S. Chen, J.H. Wu, H.Y. Zhang, M.C. Qin, X.H. Lu, Y.F. Tu, Q.B. Meng, X. W. Zhan, Fullerene derivative anchored SnO_2 for high-performance perovskite solar cells, Energy Environ. Sci. 11 (2018) 3463–3471, https://doi.org/10.1039/c8ee02172d.

[64] Q. Jiang, L.Q. Zhang, H.L. Wang, X.L. Yang, J.H. Meng, H. Liu, Z.G. Yin, J.L. Wu, X. W. Zhang, J.B. You, Enhanced electron extraction using SnO_2 for high-efciency planar-structure $HC(NH_2)_2PbI_3$-based perovskite solar cells, Nat. Energy 2 (2017) 16177, https://doi.org/10.1038/nenergy.2016.177.

[65] X.X. Jiang, Y.L. Xiong, Z.H. Zhang, Y.G. Rong, A.Y. Mei, C.B. Tian, J. Zhang, Y. M. Zhang, Y.X. Jin, H.W. Han, Q.G. Liu, Efficient hole-conductor-free printable mesoscopic perovskite solar cells based on SnO_2 compact layer, Electrochim. Acta 263 (2018) 134–139, https://doi.org/10.1016/j.electacta.2018.01.017.

[66] Y.Q. Ai, W.Q. Liu, C.H. Shou, J. Yan, N. Li, Z.H. Yang, W. Song, B.J. Yan, J. Sheng, J.C. Ye, SnO_2 surface defects tuned by $(NH_4)_2S$ for high-efficiency perovskite solar cells, Sol. Energy 194 (2019) 541–547, https://doi.org/10.1016/j.solener.2019.11.004.

[67] J.H. Heo, H.J. Han, D. Kim, T.K. Ahn, S.H. Im, Hysteresis-less inverted $CH_3NH_3PbI_3$ planar perovskite hybrid solar cells with 18.1% power conversion efficiency, Energy Environ. Sci. 8 (2015) 1602–1608, https://doi.org/10.1039/c5ee00120j.

[68] S.V. Reenen, M. Kemerink, H.J. Snaith, Modeling anomalous hysteresis in perovskite solar cells, J Phys. Chem. Lett. 6 (2015) 3808–3814, https://doi.org/10.1021/acs.jpclett.5b01645.

[69] P.Q. Song, L. Shen, L.F. Zheng, K.K. Liu, W.J. Tian, J.F. Chen, Y.J. Luo, C.B. Tian, L. Q. Xie, Z.H. Wei, Double-layered SnO_2/NH_4Cl-SnO_2 for efficient planar perovskite solar cells with improved operational stability, Nano Sel. 2 (2021) 1779–1787, https://doi.org/10.1002/nano.202000306.

[70] Y. Zhou, Z.B. Zhang, Y.Y. Cai, H. Liu, Q.Q. Qin, Q.D. Tai, X.B. Lu, X.S. Gao, L. L. Shui, S.J. Wu, J.M. Liu, High performance planar perovskite solar cells based on $CH_3NH_3PbI_{3-x}(SCN)_x$ perovskite film and SnO_2 electron transport layer prepared in ambient air with 70% humility, Electrochim. Acta 260 (2018) 468–476, https://doi.org/10.1016/j.electacta.2017.12.076.